Journal of Power Sources 238 (2013) 57–64

Contents lists available at SciVerse ScienceDirect

Journal of Power Sources

journal homepage: www.elsevier.com/locate/jpowsour

Oxidative steam reforming of ethanol over Rh catalyst supported on $Ce_{1-x}La_xO_y$ ($x = 0.3$) solid solution prepared by urea co-precipitation method

Xue Han, Yunbo Yu*, Hong He, Jiaojiao Zhao, Yafei Wang

Research Center for Eco-Environmental Sciences, Chinese Academy of Sciences, 18 Shuangqing Road, Haidian District, Beijing 100085, China

HIGHLIGHTS

- Ce–La solid solution supported Rh catalyst shows high activity for H_2 production.
- The catalyst also shows low CO selectivity and good stability.
- The performance of the catalysts varied depending on urea/metal ratio during preparation.

GRAPHICAL ABSTRACT

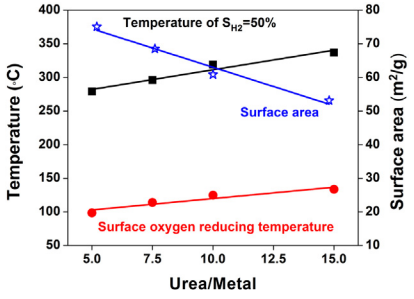

ARTICLE INFO

Article history:
Received 7 December 2012
Received in revised form
4 March 2013
Accepted 6 March 2013
Available online 19 March 2013

Keywords:
Hydrogen production
Ethanol
Oxidative steam reforming
Cerium–Lanthanum solid solution
Urea co-precipitation
Rhodium catalysts

ABSTRACT

A $Ce_{1-x}La_xO_y$ solid solution (CL) is prepared by a co-precipitation method using urea as a precipitant, with varying urea/metal molar ratio (N). The supported rhodium catalysts are then prepared by an impregnation method for use in hydrogen production from oxidative steam reforming (OSR) of ethanol. X-ray diffraction and Raman spectra results confirm the formation of CL, and the crystal structures of these catalysts are not very sensitive to the urea/metal molar ratios ($N = 5$–15). However, the surface area and reducibility of the Rh/CL-N catalysts decrease monotonically with increasing N. During the OSR process, a similar tendency is also observed for ethanol conversion and hydrogen selectivity. Among the catalysts tested, Rh/CL-5 shows the best catalytic performance, achieving >97% ethanol conversion at 300 °C with H_2 yield rate of 210 μmol g-cat^{-1} s^{-1}. At 450 °C, its hydrogen selectivity reaches 117%, with no observable change after 72 h aging.

1. Introduction

Hydrogen-powered fuel cell vehicles have recently attracted increasing attention because of their high energy efficiency and minor environmental impact [1–3]. Bio-ethanol is an ideal chemical carrier of hydrogen for several reasons [4–8]: (1) it can be derived from renewable biomass resources that make the production of hydrogen sustainable; (2) except for methanol, which is more toxic, ethanol's hydrogen/carbon ratio is higher than that of other liquid hydrocarbons or oxygenates; (3) it is free from catalyst poisons such as sulfur; (4) it is easy to transport and biodegradable. In order to power vehicles by hydrogen energy produced from ethanol, oxidative steam reforming (OSR) of ethanol has been widely investigated due to its properties of high ethanol conversion and H_2 selectivity [9], low coke deposition [1], CO selectivity [10] and heat supply [11] at low temperatures.

* Corresponding author. Tel./fax: +86 10 62849121.
E-mail address: ybyu@rcees.ac.cn (Y. Yu).

0378-7753/$ – see front matter © 2013 Elsevier B.V. All rights reserved.
http://dx.doi.org/10.1016/j.jpowsour.2013.03.032

For the OSR of ethanol, an increasing number of papers report the use of ceria-supported Rh (Rh/CeO_2) as a candidate catalyst [4,5,12–14]. This is mainly because redox supports such as ceria and ceria-containing mixed oxides improve catalyst stability due to their high oxygen storage/release capacity (OSC) and oxygen mobility [4,15]. To further increase the OSC and stability of ceria-containing catalysts, ceria is frequently combined with other metal ions to create solid solutions [16]. Reddy et al. confirmed that La^{3+} doping greatly increased the OSC value of ceria because more oxygen vacancies were created by substitution of Ce^{4+} cations with La^{3+}cations [17]. The oxygen vacancies also helped ceria to create a strong metal-support interaction, and hence, promote the dispersion of noble metals [18–20]. La doping also enhanced the activity and stability against sintering of ceria-supported noble metal catalysts for low temperature WGS, giving an opportunity for lowering the concentration of CO in H_2 production [21,22]. The presence of CO degrades the performance of Pt electrodes in fuel cell systems [13,14].

$Ce_{1-x}La_xO_y$ solid solutions (CL) can be prepared by citric acid sol–gel [23], mechanically mixed high-temperature solid state reaction [24,25], traditional co-precipitation [17], well-controlled NH_4HCO_3 co-precipitation [26,27] and the urea decomposition by co-precipitation method [22,28]. Among them, the urea co-precipitation method is extensively applied because it is a simple environmental friendly method [29] and good catalytic performance is frequently obtained with ceria-containing mixed oxides [30].

In this work, $Ce_{1-x}La_xO_y$ ($x = 0.3$) solid solution supports were prepared by a co-precipitation method using urea as a precipitant with varying urea/metal molar ratios ($N = 2.5$, 5, 7.5, 10, 15). 1 wt.% Rh catalysts supported on CL-N ($CL = Ce_{0.7}La_{0.3}O_y$) were then prepared by an impregnation method for use in hydrogen production by OSR of ethanol. It was found that the urea/metal molar ratio had a significant influence on the catalytic performance of Rh/CL-N catalysts for the OSR of ethanol.

2. Experimental

2.1. Catalyst preparation

$Ce_{1-x}La_xO_y$ solid solution supports were prepared by the urea co-precipitation method with varying urea/metal mole ratio ($N = 2.5$, 5, 7.5, 10, 15). Typically, 0.07 mol cerium (III) nitrate hexahydrate ($Ce(NO_3)_3\cdot 6H_2O$, 99%) and 0.03 mol lanthanum (III) nitrate hexahydrate ($La(NO_3)_3\cdot 6H_2O$, 98%) were placed into 200 mL water together with urea, and then stirred for 24 h. The precipitate was dried at 100 °C for 12 h, and then thermally treated in a furnace at 500 °C for 5 h in air. The supported rhodium catalysts were prepared by impregnation, then were dried at 100 °C for 12 h and calcined at 500 °C for 3 h in air. Rhodium loading was fixed at 1 wt.% and the precursor was $RhCl_3\cdot 3H_2O$. The 1%Rh/CeO_2 (Rh/C) with $N = 5$ was also prepared as a reference in the crystal structure analysis.

2.2. Characterization

The BET (Brunauer, Emmett, and Teller) surface areas of catalysts were determined on Autosorb iQ-1MP automatic equipment by physical adsorption measurements with N_2 at −196 °C. Prior to N_2 physical sorption, the samples were degassed at 300 °C for 3 h.

The chemical composition of the catalyst was determined by inductively coupled plasma atomic emission spectroscopy (ICP-AES) using an OPTIMA 2000DV spectrometer.

X-ray powder diffraction (XRD) patterns were measured using a PANalytical X'Pert Pro diffractometer with Cu Kα ($\lambda = 0.15406$ nm) radiation. The data were collected for 2θ from 10 to 90° at 5° min^{-1} with a step size of 0.026°. The structure was refined using Rietveld analysis.

Raman spectra of the catalysts were recorded at room temperature on a UV resonance Raman spectrometer (UVR DLPC-DL-03). A continuous diode-pumped solid state (DPSS) laser beam (532 nm) was used as the exciting radiation and the power output was about 48 mW. The instrument was calibrated against the Stokes Raman signal of Teflon at 1378 cm^{-1}. The diameter of the laser spot on the sample surface was focused at 25 μm. The spectral resolution was 2.0 cm^{-1}. All Raman spectra used in this paper were original and unsmoothed.

The surface morphologies of catalysts were studied using a S-3000N Scanning Electron Microscope (SEM). Prior to observation, the samples were coated with a thin Au film to avoid any charge accumulation on the sample surface and to improve the image contrast.

X-ray photoelectron spectra (XPS) were recorded in a scanning X-ray microprobe (AXIS Ultra, Kratos Analytical, Inc.) using Al Kα radiation. Binding energies were calibrated using C 1s (BE = 284.8 eV) as standard.

Hydrogen temperature-programmed reduction (H_2-TPR) measurements were carried out in a conventional set-up equipped with a thermal conductivity detector (TCD). Samples (200 mg) were heated from room temperature to 900 °C in a reducing gas mixture (10 vol.% H_2/He, 50 mL min^{-1}) at a ramp rate of 10 °C min^{-1}.

2.3. Catalytic measurements

The OSR reaction of ethanol was carried out in a continuous-flow fixed-bed micro-reactor made of a quartz tube 6 mm in inner diameter with 100 ± 2 mg catalyst (40–60 mesh, diluted with 300 mg SiO_2). A mixture of ethanol and water was supplied by a syringe pump at a rate of 0.06 mL min^{-1}. After being sufficiently vaporized by passing through a preheating zone at 150 °C, this mixture was continuously fed into the reactor together with the N_2 carrier (300 mL min^{-1}) and O_2 ($EtOH:H_2O:O_2 = 1:3:0.5$), with a space velocity of 93 μmol g-cat^{-1} s^{-1}. The catalytic reaction was carried out from 200 °C to 450 °C with six evenly spaced temperature points and each point was maintained for at least 1.5 h. The effluent gases were analyzed on-line at a given temperature by using a gas chromatograph (Shimadzu, GC-2014C) equipped with two TCDs and one FID with carbon mass balance within 100 ± 3%.

Since this work was carried out at on-board conditions, a room temperature normal flow rate (F_x) that takes into account the volume change as a result of the reactions was considered to calculate conversions and selectivities:

$$F_x = \frac{[X] \times F_{N_2}}{[N_2]} \quad (1)$$

where F_{N2} is the N_2 flow rate under a room temperature, $[N_2]$ is the concentration of N_2 (%), and $[X]$ is the concentration of X (%). The ethanol conversion was calculated according to Equation (2) where $F_{EtOH,in}$ and $F_{EtOH,out}$ represent the normal flow rate of the ethanol measured at the inlet and at the outlet of the reactor, respectively.

$$C_{EtOH} = \frac{F_{EtOH,in} - F_{EtOH,out}}{F_{EtOH,in}} \quad (2)$$

The selectivity to carbon-containing products (S_x) was calculated according to the following equations:

$$S_x = \frac{F_x}{\alpha \times F_{EtOH,in} \times C_{EtOH}} \quad (3)$$

where α is the number of atoms of carbon in the product ($\alpha = 1$ for CO, CO_2 and CH_4; while $\alpha = 2$ for C_2H_4 and CH_3CHO).

3. Results and discussion

3.1. Physical and chemical prosperities of the Rh/CL-N catalysts

The precipitates from the urea co-precipitation method, formed by aging an aqueous solution containing cerium(III) nitrate, lanthanum-(III) nitrate and urea, were confirmed to be $Ce_{1-x}La_x(OH)CO_3$ by Jobbagy et al., exhibiting a weight loss of 20.7–24.6% to produce CL solid solution [28]. By using thermal gravimetric analysis, we also measured the transformation of precipitates obtained from the urea co-precipitation method. Taking Rh/CL-5 as an example, the weight change of the precipitate was about 23% within the temperature range 250–500 °C (Fig. 1), which confirmed the transformation of $Ce_{1-x}La_x(OH)CO_3$ to $Ce_{1-x}La_xO_y$. In order to ensure the transformation was totally completed, the samples were treated at 500 °C for 5 h during the calcination process. The transformation of the precipitates from the urea co-precipitation method can be described as follows:

$$\frac{1-x}{2}O_2 + 2Ce_{1-x}La_x(OH)CO_3 \rightarrow 2Ce_{1-x}La_xO_y + H_2O + 2CO_2 \quad (4)$$

In theory, If 0.07 mol $Ce(NO_3)_3\cdot 6H_2O$ and 0.03 mol $La(NO_3)_3\cdot 6H_2O$ were employed to produce $Ce_{1-x}La_xO_y$ ($Ce_{0.7}La_{0.3}O_{1.85}$), the weight of product would be 16.93 g. Based on this, the experimental yields of $Ce_{1-x}La_xO_y$ with different urea/metal molar ratios can be obtained (Fig. 2A). In the case of urea/metal = 2.5, the yield of $Ce_{1-x}La_xO_y$ was only about 40%, which means more than half of these rare earth elements were wasted. As for urea/metal ≧ 5, the yield of $Ce_{1-x}La_xO_y$ slowly increased with urea/metal ratio from 87.1% to 94.5%. Considering the loss during preparation, this indicates that most of the Ce and La was precipitated.

The surface areas of the Rh/CL-*N* catalysts are shown Fig. 2B. Except for Rh/CL-2.5, the samples' surface areas decreased linearly from 75 $m^2\ g^{-1}$ to 53 $m^2\ g^{-1}$ with increasing urea/metal mol ratio. This means the surface area of samples can be accurately controlled by the concentration of precipitant during the preparation of supports by urea co-precipitation. Fig. 2C and D shows that the average pore diameter and total pore volume increased greatly with urea/metal molar ratio (N = 5, 7.5, 10, 15).

ICP-AES analysis revealed that for all the catalysts, the bulk ratio of La/(La + Ce) was lower than the designed value (x = 0.3), especially when urea/metal = 2.5 (Fig. 3). Combined with the precipitate weight data, it is clear that precipitation of Ce is favored comparing to La. The La/(La + Ce) values of the Rh/CL-*N* catalysts (N = 5, 7.5, 10, 15) changed from 26.2 to 29.6 and these can be taken as similar chemical compositions. Considering the significantly lower La/(La + Ce) of Rh/CL-2.5 compared to the other four catalysts and the massive waste of precursor, we will not focus on it in the following discussion.

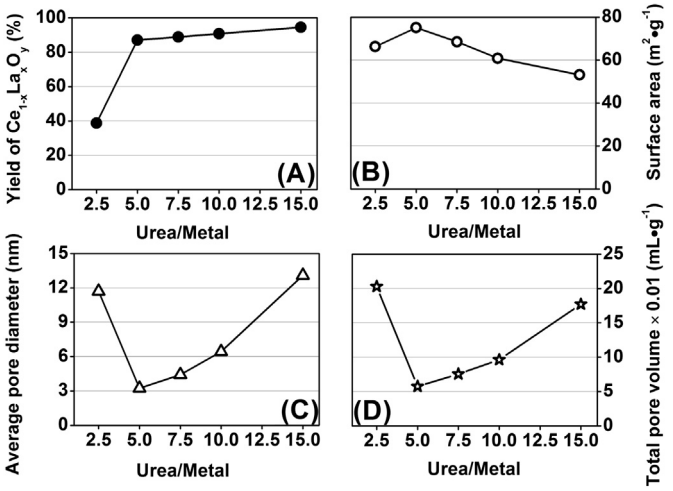

Fig. 2. Physical prosperities of the Rh/CL-*N* catalysts. (A) Yield of $Ce_{1-x}La_xO_y$ with different urea/metal molar ratio, (B), (C), (D) surface area, average pore diameter and total pore volume from BET tests.

The surface La/(La + Ce) of the catalysts were also calculated from the XPS results and summarized in Fig. 3. It was observed that the content of La on the surface was a little higher than that in the bulk, which means the surface was slightly enriched with La^{3+} [17,25]. With increase in precipitant concentration, the surface enrichment of La was more pronounced. The segregation of the La on the surface of the samples is probably due to the difference in the hydrolysis rate [17].

Fig. 4 shows the SEM images of Rh/CL-*N* (N = 5, 7.5, 10, 15) catalysts calcined at 500 °C. At low urea/metal molar ratio (N = 5 and 7.5), the catalysts exhibited a cracked triangular-prism-like surface morphology. With increasing urea/metal mol ratio (N), however, the surface morphology of Rh/CL-10 and Rh/CL-15 became floccular in nature. This means the concentration of precipitant during the preparation of supports can also greatly affect the surface morphology of the catalyst.

3.2. Crystal structure of Rh/CL-N catalysts

Fig. 5 presents the XRD patterns of Rh/CL-*N* (N = 5, 7.5, 10, 15) catalysts and that of Rh supported on pure ceria (Rh/C) catalysts.

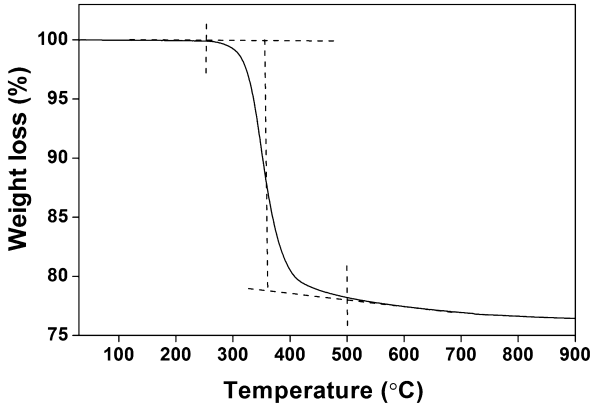

Fig. 1. The weight loss during the thermal decomposition of $Ce_{0.7}La_{0.3}(OH)CO_3$ (N = 5) from 30 °C to 900 °C (2 °C min^{-1}) under the air condition.

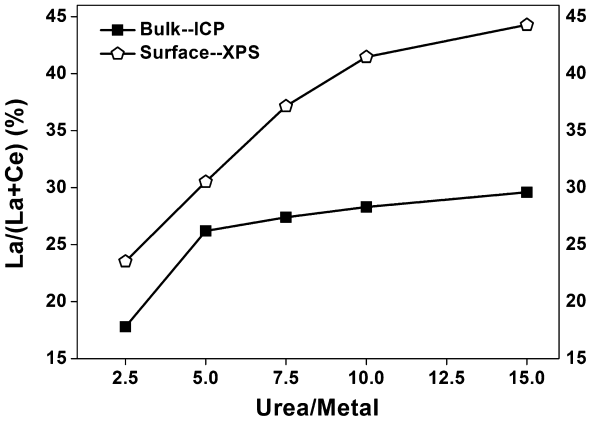

Fig. 3. The La/(La + Ce) molar ratios of catalysts measured by ICP and XPS methods.

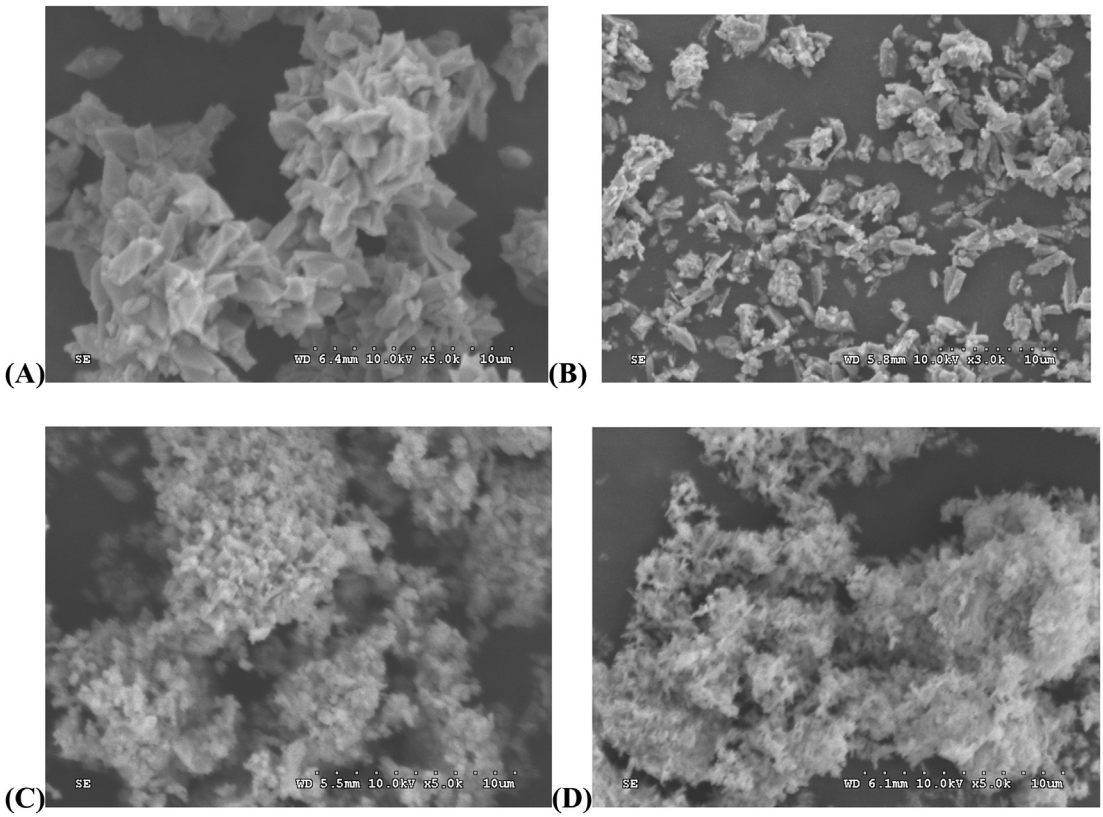

Fig. 4. SEM images of Rh/CL-5 (A), Rh/CL-7.5 (B), Rh/CL-10 (C) and Rh/CL (D) catalysts calcined at 500 °C.

These all exhibited the characteristic diffractogram of the fluorite cubic structure of CeO_2 (JCPDS 34-0394) [23,28], while no peaks due to La compounds were observed. From the XRD patterns it could be noted that doping of ceria with La^{3+} led to broadening and shifting of diffraction peaks toward lower angles as well as lower diffraction intensity. This shift can be explained as due to the partial substitution of Ce^{4+} with La^{3+}. Considering that the ionic radius of La^{3+} (0.11 nm) is larger than Ce^{4+} (0.097 nm), incorporation of La^{3+} into the CeO_2 lattice will result in lattice expansion of CeO_2 [17]. The calculated cell parameter "a" of Rh/CL-*N* catalysts was increasing slowly with *N* and La content from 0.5473 to 0.5489 nm, which were calculated after structure refine by Rietveld analysis (Table 1). The cell parameters of Rh/Cl-*N* catalysts are clearly larger than that of pure ceria (a = 0.541 nm). These results indicate that a solid solution of $Ce_{1-x}La_xO_y$ was formed by introducing La^{3+} into the lattice of ceria. The average particle diameters of the Rh/CL-*N* catalysts were in the range of 9.2–9.3 nm, which were calculated by applying the Scherrer equation to the characteristic (111), (200), (220) peaks of CeO_2 from the XRD results after structure refinement. Therefore, the above results indicate that all of the Rh/CL-*N* catalysts had similar ceria fluorite cubic structures with a certain extent of deformation, and the average particle diameters of these catalysts were not sensitive to the urea/metal molar ratio (*N*), when the chemical composition (La/(Ce + La)) was similar.

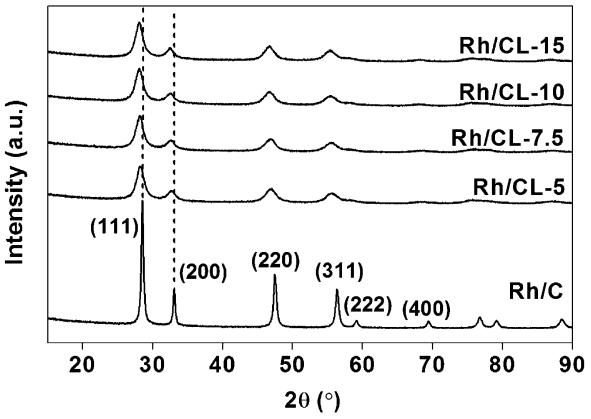

Fig. 5. XRD patterns of the Rh/CL-*N* catalysts.

Raman spectroscopy is a useful technique to derive information on the oxygen vacancies of oxide materials, especially ceria-containing solid solutions. The Raman results pertaining to Rh/CL-*N* (N = 5, 7.5, 10, 15) catalysts along with Rh/C are shown in Fig. 6. A strong band at ~460 cm^{-1} corresponding to the triply degenerate F_{2g} mode of fluorite CeO_2 is observed for all of the samples. The F_{2g} band, viewed as the symmetric breathing mode of the oxygen ions surrounded by cations, is sensitive to any disorder in the oxygen sub-lattice, the presence of which indicates that La^{3+}-

Table 1
The particle size estimated from predominant crystalline planes by the Scherrer equation and cell parameter a of Rh/CL-*N* catalysts. The structure refine by Rietveld analysis was used.

Catalysts	Particle size (nm)			Average particle size (nm)	Cell parameter a (nm)
	(111)	(200)	(220)		
Rh/CL-5	9.5	9.3	8.8	9.2	0.5473
Rh/CL-7.5	9.6	9.3	8.8	9.2	0.5479
Rh/CL-10	9.5	9.2	8.9	9.2	0.5484
Rh/CL-15	9.6	9.4	9.0	9.3	0.5489

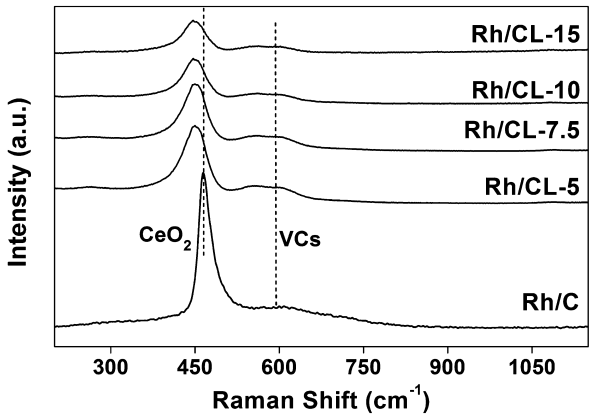

Fig. 6. Raman spectra of Rh/CL-*N* catalysts.

doped ceria exhibits a cubic fluorite type structure [17]. As ceria is doped with La^{3+}, the F_{2g} mode becomes asymmetric and slightly shifted to lower wavenumber, which is also a result of La^{3+} being introduced into the ceria lattice. There were no significant bond shifts within the La-containing catalysts, which further confirmed that the urea/metal ratio does not deeply affect the lattice structure of Ce–La solid solutions. Considering that the band at ~1077 cm^{-1} has always been accepted as the A_{1g} mode of $La_2O_2CO_3$, and this band was not observed in La-doped ceria, indicates that a Ce–La solid solution is formed, which is consistent with the XRD results. A band at about 600 cm^{-1} was associated with oxygen vacancies (VCs), which are generated to maintain the electrostatic balance of Ce^{3+}/La^{3+}-containing fluorite ceria [17,24]. The intensity of the VCs band for La-containing samples was clearly increased compared to Rh/C.

All of the above indicated that the series of Rh/CL-*N* catalysts ($N = 5, 7.5, 10, 15$) have similar composition and lattice structure but exhibit different surface area and morphology.

3.3. Redox properties of Rh/CL-N catalysts

The objective of XPS analysis was to investigate the valence states of the components of the Rh/CL-*N* catalysts and the surface composition, which has been briefly discussed (Fig. 3). The XPS Rh 3d spectra show a doublet centered at around 309 and 314 eV (Fig. 7A). These peaks correspond to the binding energy of Rh 3d5/2 and Rh 3d3/2, respectively, with a spin orbit coupling of about 5 eV, which is close to the value for Rh^{3+} in the Rh/CL-*N* catalysts [14]. Over all the samples, no Rh structures were observed in TEM images, indicating a high dispersion of Rh (result not shown here).

The O 1s core level spectra of the Rh/CL-*N* catalysts are presented in Fig. 7B. The peak with low binding energy (529–530 eV) is attributed to the lattice oxygen ions (O^{2-}) of the crystalline network [17]. On the high binding energy side at 531.5–532 eV ($\Delta E_B \cong 2.4$ eV), different assignments have been made according to different objectives [31,32]. However, it has been acknowledged that the high binding energy peak corresponds to oxygen species located on the surface and more easily reduced by H_2. Therefore, we call this species "surface oxygen" (O_S), and calculated its percentage contribution to total oxygen ($O_T = O^{2-} + O_S$), as summarized in Table 2 along with lattice oxygen. The bulk oxygen percentage order of the catalysts series is Rh/CL-10 < Rh/CL-15 < Rh/CL-7.5 < Rh/CL-5.

The splitting pattern of the La 3d core level spectra is shown in Fig. 7C. The splitting is due to spin orbit interaction and charge transfer from ligand (O 2p) to metal (La 4f) and the splitting energy from the spectra is about 4.3 eV [17]. Note that with different urea/

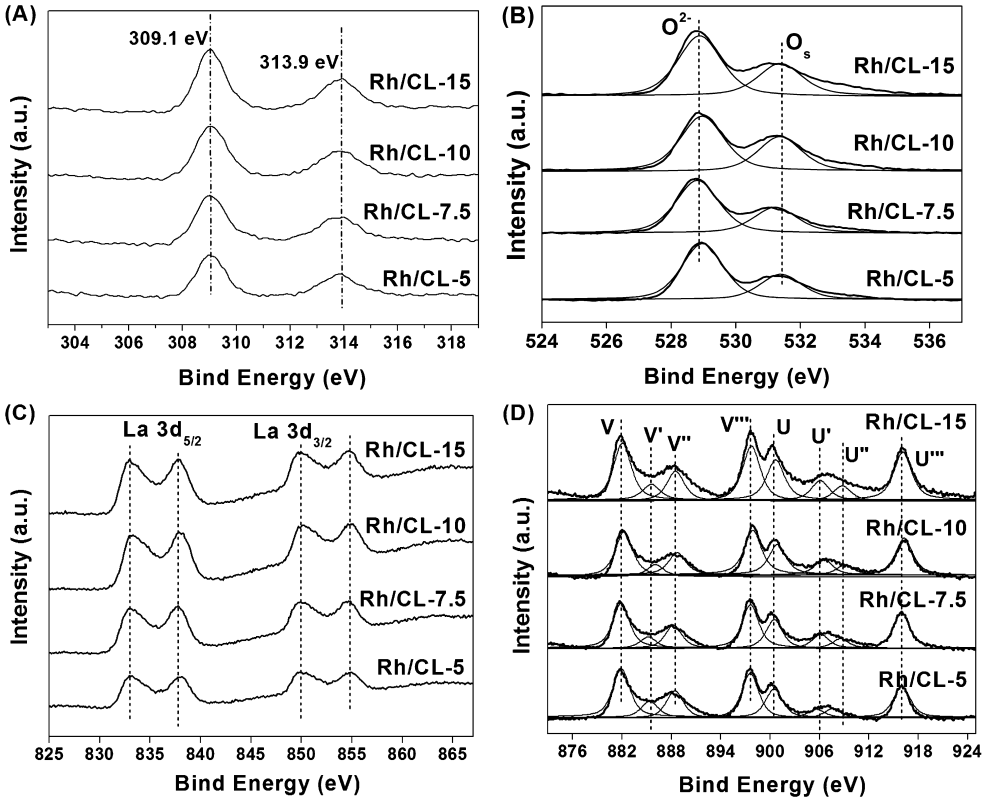

Fig. 7. XPS profiles of Rh 3d (A), O 1s (B), La 3d (C) and Ce 3d (D) of Rh/CL-*N* catalysts.

Table 2
XPS O1s and Ce 3d data measured for the Rh/CL-*N*.

	E (eV)		O/O_T(%)		$Ce^{M+}/(Ce + La)$/%	
	O_S	O^{2-}	O_S/O_T	O^{2-}/O_T	$Ce^{3+}/(Ce^{3+}+Ce^{4+})$	$(Ce^{3+}+La^{3+})/(Ce + La)$
Rh/CL-5	531.4	528.9	30.9	69.1	31.9	52.7
Rh/CL-7.5	531.3	528.8	32.6	67.4	32.8	57.8
Rh/CL-10	531.4	528.9	38.9	61.1	33.4	61.0
Rh/L-15	531.4	528.9	34.6	65.4	32.3	62.3

metal molar ratio, there is no change in position of the La 3d core level peaks. The pattern of Rh/CL-5 has slightly lower intensity is because of the lower surface La content.

Fig. 7D shows the Ce 3d XPS spectra of the Rh/CL*x* catalysts, together with the corresponding peak-fitting results. The $Ce^{3+}/(Ce^{3+} + Ce^{4+})$ and $(Ce^{3+} + La^{3+})/(Ce + La)$ ratios were calculated by analysis of the integrated peak areas of Ce^{3+} and Ce^{4+}, and the results are shown in Table 2 as well. Note that the $(Ce^{3+} + La^{3+})/(Ce + La)$ ratio in Rh/CL-*N* catalysts increased with increasing urea/metal mol ratio but the $Ce^{3+}/(Ce^{3+} + Ce^{4+})$ remained similar. These findings further confirm the La enrichment on the surface, which is also mentioned in Fig. 3.

H_2 temperature-programmed reduction (H_2-TPR) experiments are commonly used to analyze the redox properties of catalysts. The reduction profiles of Rh/CL-*N* ($N = 5, 7.5, 10, 15$) catalysts are shown in Fig. 8. There are two typical peak reduction profiles, located at 98–134 °C and 240–295 °C, respectively. The reduction temperature and H_2 consumption are summarized in Table 3. The amount of hydrogen consumed at low temperatures was in the range of 0.518–0.554 mmol g^{-1}, which was much larger than the amount needed for the reduction of Rh_2O_3 to Rh (0.146 mmol g^{-1} for 1 wt.% Rh). It seemed that the low temperature peak is related to the reduction of Rh^{3+} in Rh_2O_3, combined with the reduction of surface Ce^{4+} at the interface with Rh_2O_3 (denoted as reducible surface species, thereafter). Note that the low temperature hydrogen consumption was unchanged within 6.7%; while the reduction temperature increased noticeably from 98 to 134 °C. These findings mean that the catalysts with different N had similar low temperature hydrogen consumption but different reduction temperatures. It is also worth mentioning that the peak shape of the triangular-prism-like catalysts (Rh/CL-5 and Rh/CL-7.5) was short and fat while the shape of the floccular catalysts (Rh/CL-10 and Rh/CL-15) was tall and thin. The high-temperature peak is attributed to the reduction of bulk oxygen of CeO_2-like catalysts. However, the Rh/CL-10 catalyst that showed the least bulk oxygen in the XPS

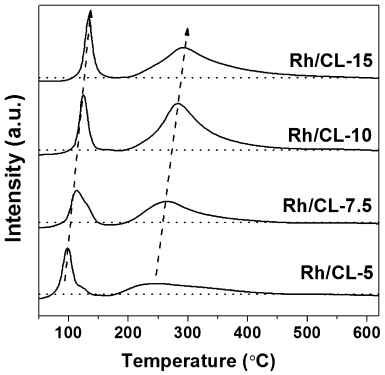

Fig. 8. H_2-TPR of the Rh/CL-*N* catalysts.

Table 3
Reduction temperature and H_2 consumption in the H_2-TPR tests.

	Reduction temperature		H_2 consumption	
	T_{low} (°C)	T_{high} (°C)	C_{low} (mmol g^{-1})	C_{high} (mmol g^{-1})
Rh/CL-5	98.4	240.6	0.554	1.138
Rh/CL-7.5	113.9	264.3	0.540	1.397
Rh/CL-10	124.8	283.6	0.549	2.143
Rh/CL-15	133.5	294.3	0.518	1.741

analysis had the highest bulk oxygen in the H_2-TPR results. This can be explained by noting that hydrogen can spill over from the supported noble metal to surface ceria and then further flow to bulk ceria, because there is no difference between surface and bulk reduction when ceria is isothermally treated [33]. Therefore, the mobility of hydrogen among the reducible species might be more important than the number of reducible species. The Rh/CL-5 catalyst had the lowest reduction temperature in the catalyst series, which shows that it is more easily reduced than other samples.

3.4. Catalytic performance of Rh/CL-N in OSR of ethanol

The above discussion indicates that the Rh/CL-*N* catalysts have similar chemical composition and crystal structure but different surface area, redox properties and SEM morphology. In the OSR reaction, ethanol conversion and product selectivity at different temperatures are shown in Fig. 9. Over the whole tested temperature region (200–450 °C), the ethanol conversion and H_2 selectivity were found to drop in the sequence: Rh/CL-5 > Rh/CL-7.5 > Rh/CL-10 > Rh/CL-15, decreasing with increasing urea/metal mole ratio. Combined with Fig. 2, this shows that a high urea/metal molar ratio will result in decreasing surface area, H_2 selectivity and reducibility for the catalysts.

Fig. 9 also shows the product distribution. In the whole temperature range, ethylene and acetone, which can easily convert to coke deposits and result in catalyst deactivation [34], were undetected (<100 ppm, not shown). CO is a poison to Pt electrodes; for Rh/CL-5 catalysts, at 400 °C the CO selectivity was lower than 2%, which means it can be directly used by phosphoric acid fuel cells (PAFC) without needing a CO-cleanup reactor [35]. Furthermore, the CO selectivity for Rh/CL-5 and Rh/CL-7.5 catalysts was clearly lower than that of Rh/CL-10 and Rh/CL-15. Considering the SEM results that were shown in Fig. 4, the triangular-prism-like catalysts produced less CO; while the CO selectivity of floccular catalysts was much higher. The relationship between surface morphology and product distribution has been barely reported for this hydrogen production reaction, and it will be further discussed in our future research.

The above discussion shows that the Rh/CL-5 catalyst showed the highest ethanol conversion and H_2 selectivity. At 300 °C, the ethanol conversion already reached 97% with H_2 yield rate of 210 μmol g-cat^{-1} s^{-1}, which is hard to reach at this low temperature even for noble metal catalysts [14,36]. At 350 °C, it achieved total ethanol conversion with CO selectivity <7%, and the H_2 yield rate was 253 μmol g-cat^{-1} s^{-1}, which is about one order of magnitude higher than that of other Rh-containing catalysts reported at the same temperature under similar reaction conditions [35,37,38]. The stability of the Rh/CL-5 catalyst during on-stream operation has also been examined at 450 °C for 72 h (Fig. 10).

For the whole time range, the catalyst showed very good stability, as no deactivation was observed. At low temperature, coke deposition induced by the formation of ethylene and acetone is the main reason for deactivation of catalysts in H_2 production from ethanol [34]. Considering ethylene and acetone were undetected over the Rh/CL-5 catalyst, its good stability is understandable.

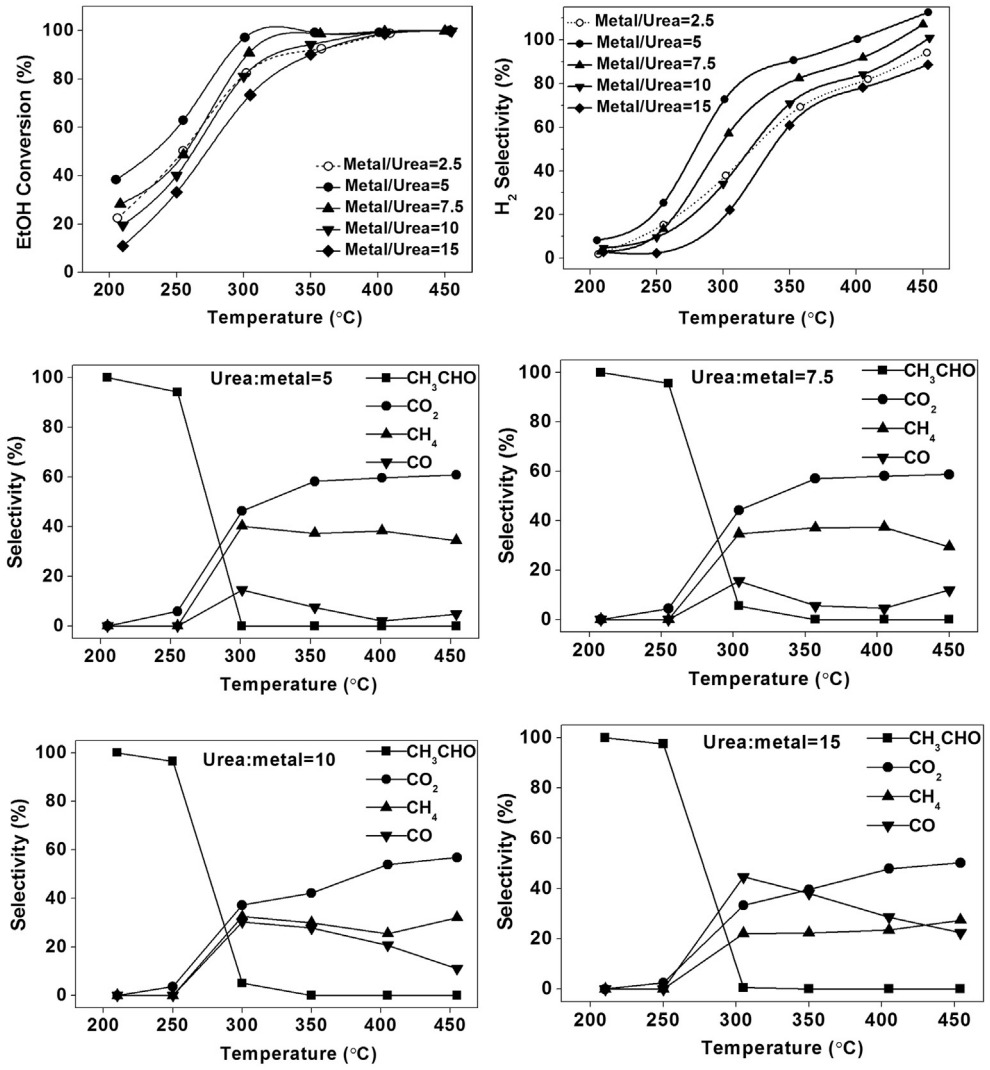

Fig. 9. Ethanol conversions and products selectivities of catalysts during the OSR reaction. Reaction conditions: catalysts weight 100 mg (40–60 mesh), ethanol:H_2O:O_2 = 1:3:0.5, N_2 = 300 mL min^{-1}, space velocity = 93 μmol g-cat^{-1} s^{-1}.

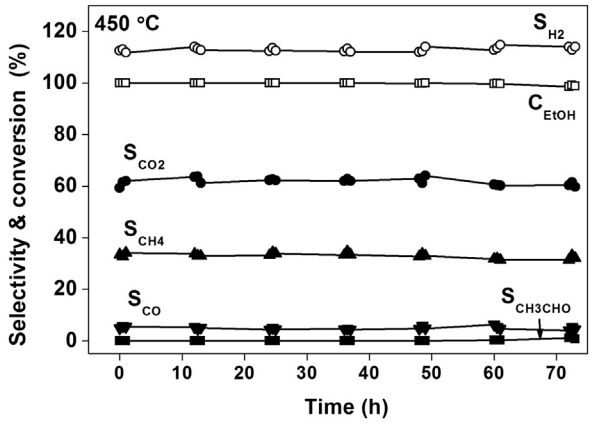

Fig. 10. Stability of Rh/CL-5 catalyst in OSR reason at 450 °C. Reaction conditions are the same as Fig. 9.

4. Conclusions

$Ce_{1-x}La_xO_y$ (x = 0.3) solid solutions were successfully prepared by a urea co-precipitation method with varying urea/metal molar ratio (N). The Rh/CL-N (N = 5, 7.5, 10, 15) catalysts have similar chemical compositions and fluorite cubic crystal structure but exhibit different SEM morphology. The surface area decreases with increasing N, which results in a decrease of redox properties, ethanol conversion and hydrogen selectivity. The Rh/CL-5 catalyst with the best hydrogen selectivity showed ethanol conversion above 97% at 300 °C and was able to maintain stability as long as 72 h at 450 °C. The $Ce_{1-x}La_xO_y$ solid solution-supported Rh catalyst is a new suitable hydrogen production catalyst and increasing its surface area by controlling the preparation conditions is a feasible way to obtain better catalyst.

Acknowledgments

We acknowledge financial support from the National Basic Research Program of China (2010CB732304) and the National Natural Science Foundation of China (21177142 and 20973193).

References

[1] G. Rabenstein, V. Hacker, J. Power Sources 185 (2008) 1293–1304.
[2] A. Haryanto, S. Fernando, N. Murali, S. Adhikari, Energy Fuels 19 (2005) 2098–2106.

[3] V. Fierro, O. Akdim, H. Provendier, C. Mirodatos, J. Power Sources 145 (2005) 659–666.
[4] L.V. Mattos, G. Jacobs, B.H. Davis, F.B. Noronha, Chem. Rev. 112 (2012) 4094–4123.
[5] M. Ni, D.Y.C. Leung, M.K.H. Leung, Int. J. Hydrogen Energy 32 (2007) 3238–3247.
[6] V.M. Garcia, M. Serra, J. Llorca, J. Power Sources 196 (2011) 4411–4417.
[7] L.P.R. Profeti, J.A.C. Dias, J.M. Assaf, E.M. Assaf, J. Power Sources 190 (2009) 525–533.
[8] M. Liao, W. Wang, R. Ran, Z. Shao, J. Power Sources 196 (2011) 6177–6185.
[9] J. Kugai, S. Velu, C. Song, Catal. Lett. 101 (2005) 255–264.
[10] L. Huang, R. Chen, D. Chu, A.T. Hsu, Int. J. Hydrogen Energy 35 (2010) 1138–1146.
[11] M. Youn, J. Seo, P. Kim, J. Kim, H. Lee, I. Song, J. Power Sources 162 (2006) 1270–1274.
[12] H. Idriss, Platinum Met. Rev. 48 (2004) 105–115.
[13] G.A. Deluga, J.R. Salge, L.D. Schmidt, X.E. Verykios, Science 303 (2004) 993–997.
[14] J. Kugai, V. Subramani, C. Song, M. Engelhard, Y. Chin, J. Catal. 238 (2006) 430–440.
[15] H. Song, U.S. Ozkan, J. Catal. 261 (2009) 66–74.
[16] C. Diagne, H. Idriss, A. Kiennemann, Catal. Commun. 3 (2002) 565–571.
[17] B.M. Reddy, L. Katta, G. Thrimurthulu, Chem. Mater. 22 (2010) 467–475.
[18] J.A. Rodriguez, S. Ma, P. Liu, J. Hrbek, J. Evans, M. Pérez, Science 318 (2007) 1757–1760.
[19] F. Wang, W. Cai, H. Provendier, Y. Schuurman, C. Descorme, C. Mirodatos, W. Shen, Int. J. Hydrogen Energy 36 (2011) 13566–13574.
[20] H.V. Fajardo, L.F.D. Probst, N.L.V. Carreño, I.T.S. Garcia, A. Valentini, Catal. Lett. 119 (2007) 228–236.
[21] F.C. Meunier, D. Reid, A. Goguet, S. Shekhtman, C. Hardacre, R. Burch, W. Deng, M. Flytzani-Stephanopoulos, J. Catal. 247 (2007) 277–287.
[22] Q. Fu, H. Saltsburg, M. Flytzani-Stephanopoulos, Science 301 (2003) 935–938.
[23] B. Zhang, D. Li, X. Wang, Catal. Today 158 (2010) 348–353.
[24] A. Bueno-Lopez, K. Krishna, M. Makkee, J.A. Moulijn, J. Catal. 230 (2005) 237–248.
[25] V. Bellière, G. Joorst, O. Stephan, F.M.F. de Groot, B.M. Weckhuysen, J. Phys. Chem. B 110 (2006) 9984–9990.
[26] M.F. Wilkes, P. Hayden, A.K. Bhattacharya, Appl. Surf. Sci. 206 (2003) 12–19.
[27] M.F. Wilkes, P. Hayden, A.K. Bhattacharya, J. Catal. 219 (2003) 286–294.
[28] M. Jobbagy, C. Sorbello, E.E. Sileo, J. Phys. Chem. C 113 (2009) 10853–10857.
[29] J.M. Campelo, D. Luna, R. Luque, J.M. Marinas, A.A. Romero, ChemSusChem 2 (2009) 18–45.
[30] W.P. Shan, F.D. Liu, H. He, X.Y. Shi, C.B. Zhang, Chem. Commun. 47 (2011) 8046–8048.
[31] J.-C. Dupin, D. Gonbeau, P. Vinatier, A. Levasseur, Phys. Chem. Chem. Phys. 2 (2000) 1319–1324.
[32] P. Ji, J. Zhang, F. Chen, M. Anpo, J. Phys. Chem. C 112 (2008) 17809–17813.
[33] A. Trovarelli, Catal. Rev. 38 (1996) 439–520.
[34] B. Zhang, W. Cai, Y. Li, Y. Xu, W. Shen, Int. J. Hydrogen Energy 33 (2008) 4377–4386.
[35] L. Chen, C.K.S. Choong, Z. Zhong, L. Huang, T.P. Ang, L. Hong, J. Lin, J. Catal. 276 (2010) 197–200.
[36] X. Wu, S. Kawi, Energy Environ. Sci. 3 (2010) 334–342.
[37] E. Brum Pereira, P. Ramirez de la Piscina, S. Marti, N. Homs, Energy Environ. Sci. 3 (2010) 487–493.
[38] E.B. Pereira, N. Homs, S. Martí, J.L.G. Fierro, P. Ramírez de la Piscina, J. Catal. 257 (2008) 206–214.